THE JOURNAL OF PHYSICAL CHEMISTRY C
A JOURNAL OF THE AMERICAN CHEMICAL SOCIETY

pubs.acs.org/JPCC

Article

# Optimized 3D Reconstruction of Large, Compact Assemblies of Metallic Nanoparticles

*Published as part of The Journal of Physical Chemistry virtual special issue "Marie-Paule Pileni Festschrift".*

Thomas Altantzis,[⊥] Da Wang,[⊥] Ajinkya Kadu,[⊥] Alfons van Blaaderen, and Sara Bals*

Cite This: *J. Phys. Chem. C* 2021, 125, 26240–26246

Read Online

ACCESS | Metrics & More | Article Recommendations



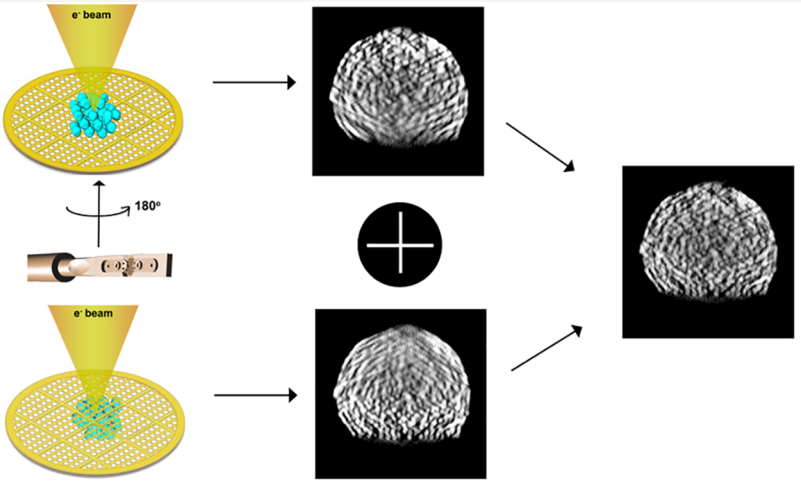


**ABSTRACT:** 3D characterization of assemblies of nanoparticles is of great importance to determine their structure−property connection. Such investigations become increasingly more challenging when the assemblies become larger and more compact. In this paper, we propose an optimized approach for electron tomography to minimize artifacts related to beam broadening in high angle annular dark-field scanning transmission electron microscopy mode. These artifacts are typically present at one side of the reconstructed 3D data set for thick nanoparticle assemblies. To overcome this problem, we propose a procedure in which two tomographic tilt series of the same sample are acquired. After acquiring the first series, the sample is flipped over 180°, and a second tilt series is acquired. By merging the two reconstructions, blurring in the reconstructed volume is minimized. Next, this approach is combined with an advanced three-dimensional reconstruction algorithm yielding quantitative structural information. Here, the approach is applied to a thick and compact assembly of spherical Au nanoparticles, but the methodology can we used to investigate a broad range of samples.

## INTRODUCTION

The controlled organization of nanoparticles (NPs) into assemblies has numerous applications in different scientific fields, including plasmonics,[1] signal enhancement,[2,3] catalysis,[4,5] and data storage.[6,7] Assemblies have gained increasing scientific interest thanks to their improved properties in comparison to those of their individual building blocks. Moreover, by modifying, e.g., the size and shape of the individual NPs, the interparticle distances or the chemical composition of the building blocks, assemblies with various shapes and functionalities have been obtained.[8,9] Since the properties of these nanostructures are inseparably connected to their three-dimensional (3D) structure and shape, a thorough structural and morphological characterization is of great importance.

Transmission electron microscopy (TEM) is an ideal technique to investigate materials at the nanometer level or even at the atomic scale. The technique has therefore been widely used in the study of nanoassemblies. However, TEM

Received: September 27, 2021
Revised: November 8, 2021
Published: November 19, 2021

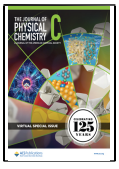




https://doi.org/10.1021/acs.jpcc.1c08478
J. Phys. Chem. C 2021, 125, 26240−26246

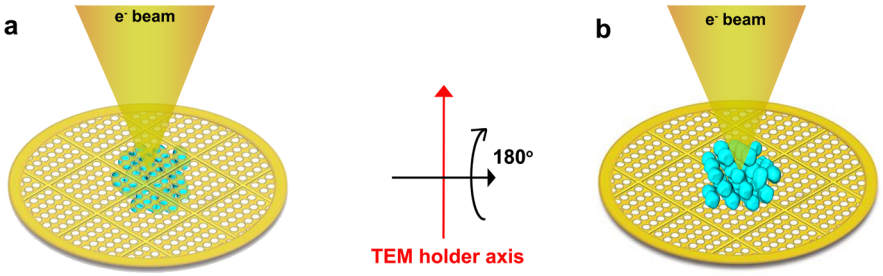


**Figure 1.** Schematic representation of the acquisition. (a) In our experiment, during the acquisition of series A, the electron beam exit surface is at the part of the assembly which is not in contact with the TEM grid. After rotating the TEM grid over 180° around the axis perpendicular to the axis of the TEM holder to acquire series B, the botttom part of the assembly, which is in contact with the TEM grid (b), becomes the electron beam exit surface. It should be noted that, in this scheme, the assembly was enlarged on purpose for a better visualization.

images only correspond to a two-dimensional (2D) projection of a 3D object. Therefore, electron tomography, a technique that derives a 3D reconstruction from a tilt series of 2D projection images, has become a standard technique to characterize nanoassemblies in 3D.[8,10−15] When assemblies of metallic nanoparticles are investigated, acquisition of electron tomography series is usually performed in high angle annular dark-field scanning TEM (HAADF-STEM) mode. In this manner, diffraction contrast present in bright-field TEM (BF-TEM) images is minimized, and the projection requirement for tomography is fulfilled.[16] For relatively small (consisting of 100 particles or less) or loose assemblies, in which the distance between the composing building blocks is rather large, conventional electron tomography techniques enable one to determine the morphology and the inner structure of the assemblies. Moreover, a manual segmentation allows one to determine, e.g., the 3D stacking of the nanoparticles in a quantitative manner.[8,10,17,18] However, when the size and density (atomic number $Z$) of the investigated assembly increase, several artifacts become dominant in the reconstruction. A well-known limitation is the so-called cupping artifact,[11] which causes an underestimation of the intensities in the middle part of 3D reconstructions of relatively thick samples. Another observation is that features near the bottom surface of the volume become blurry, which is related to the so-called top−bottom effect (TBE).[19] These artifacts arise mainly due to beam broadening from multiple elastic scattering and the missing wedge of information stemming from a limited tilt range of the sample within the pole pieces of the objective lens.

Clearly, the missing information will lead to a misinterpretation of the structure. Therefore, an optimization of the acquisition process is required. The use of BF-STEM using an axial detector was proposed as an alternative for the investigation of thick amorphous specimens.[20] Unfortunately, this approach cannot be applied to crystalline samples and compact assemblies of NPs, since BF-STEM projections are affected by diffraction contrast, which hamper a quantitative 3D analysis.[16] Furthermore, the spatial resolution provided by this approach is not sufficient to determine interparticle spacing in compact assemblies of small NPs.

In this work, we propose an optimized approach based on the acquisition of a second tilt series after flipping the sample over 180° around the axis perpendicular to the axis of the holder. As a proof of concept, we applied the approach to a 165 nm thick and compact assembly of spherical gold (Au) NPs. By merging the two reconstructions, we were able to drastically reduce the strong blurring of sample features at the bottom part of the reconstructed volume, thus enabling a reliable structural analysis. Our technique is of interest to a wide range of thick crystalline samples or nanostructures composed of elements with a high atomic number $Z$.

## MATERIALS AND METHODS

**Chemicals.** Chemicals used were dextran from *Leuconostoc mesenteroides* (Sigma-Aldrich, mol. wt. 1 500 000−2 800 000), cyclohexane (Sigma-Aldrich, 99.8%), sodium dodecyl sulfate (SDS, Sigma-Aldrich, ≥99.0%), ethanol (Baker Analyzed, ≥99.9%, absolute), anhydrous benzene (Sigma-Aldrich, 99.8%), chloro(triphenylphospine)gold(I) ($Ph_3P$)AuCl, Sigma-Aldrich, ≥ 99.0%), *tert*-butylamine−borane complex powders (Sigma-Aldrich, 97%), and 1-dodecanethiol (Sigma-Aldrich, ≥ 98%). For deionized water (DI $H_2O$), a Millipore Direct-Q UV3 reverse osmosis filter apparatus was used (18 MΩ at 25 °C).

**Synthesis.** *Au Nanocrystals Synthesis.* Here, 6.3 nm Au nanocrystals were synthesized according to a method reported in the literature with minor modifications.[21] First, 1 mmol of ($Ph_3P$)AuCl was mixed with 0.5 mL of 1-dodecanethiol in 80 mL of anhydrous benzene to form a clear solution. Then 10 mmol of *tert*-butylamine−borane complex powders were then added in one portion. The mixture was then heated upon stirring at 55 °C for 1 h before the mixture was cooled to room temperature. The synthesized Au nanocrystals were purified with the solvent/antisolvent pair cyclohexane/ethanol three times. Finally, the Au nanocrystals were weighted and redispersed in cyclohexane.

*Self-Assembly of Au Nanocrystals in Spherical Confinement.* For a typical self-assembly in a confinement experiment using the nanocrystals as explained above, 6.5 mg of 6.3 nm Au nanocrystals were dispersed in 1.0 mL of cyclohexane and added to a mixture of 400 mg of dextran and 70 mg of SDS in 10 mL of DI $H_2O$. The resulting emulsion was agitated by shear with a shear rate of $1.56 \times 10^5$ $s^{-1}$, using a Couette rotor-stator device (gap spacing 0.100 mm) following the procedure and home-built equipment described by Mason and Bibette.[22] The emulsion was then evaporated at room temperature using a VWR VV3 vortex mixer for 48 h. The resulting SPs suspension was purified by centrifugation with a relative centrifugal force of 489 $g$ for 15 min using an Eppendorf 5415C centrifuge, followed by redispersing in DI $H_2O$. The above-mentioned procedure was repeated twice.

*TEM Preparation of Au Assemblies.* To prepare a sample for electron tomography analysis, 3 μL of the Au assemblies suspension in DI $H_2O$ was deposited on a Quantifoil (2/2, 200 mesh) copper grid and plunged frozen into liquid ethane using


https://doi.org/10.1021/acs.jpcc.1c08478
J. Phys. Chem. C 2021, 125, 26240−26246

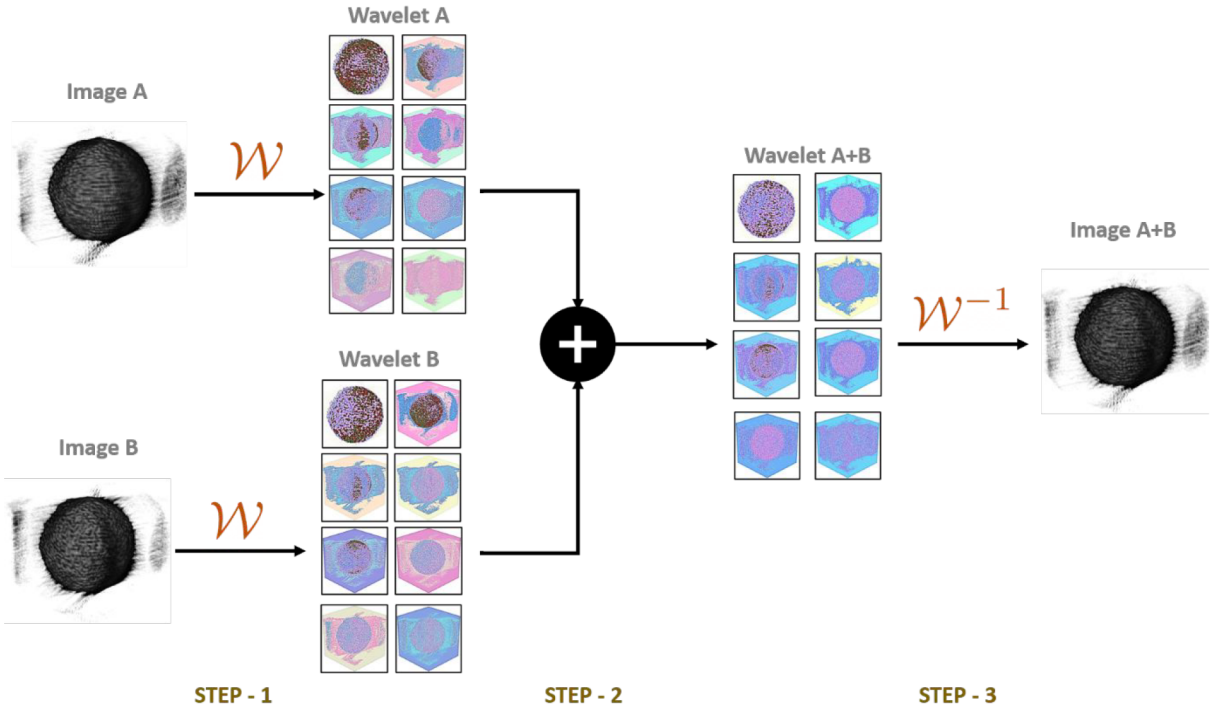


**Figure 2.** Wavelet-based image volume fusion: This approach consists of three steps: (i) Computing the wavelet decomposition of two 3D volumes, (ii) adding the elements of decompositions to produce new wavelet coefficients, and, (iii) from these new wavelet coefficients, performing the reconstruction process to obtain the fused image volume.

a Vitrobot Mark2 plunge freezer at temperatures around 90 K. The sample was then freeze-dried over a period of 8 h under vacuum at 177 K and subsequently allowed to warm up to room temperature prior to electron microscopy analysis.[15]

*Acquisition and Alignment of Tomography Tilt Series.* For assemblies of NPs, a slight shrinkage of the volume is often observed during the first minutes of illumination by the electron beam, without the internal structure of the assembly being affected. In order to prevent this during the acquisition of the tilt series, the assembly investigated here was illuminated prior to our experiments by the electron beam for a few minutes along different tilt angles, using a beam current of 40 pA. This procedure, which is often referred to as a "beam-shower", prevents sample shrinkage to occur during the acquisition of the tilt series and allows the assemblies to be stabilized in a homogeneous manner. All tilt series were acquired in HAADF-STEM mode using an aberration-corrected "cubed" Thermo Fisher Scientific-Titan electron microscope operated at 300 kV. The beam convergence and detector's inner collection semiangles were set to 8 and 62 mrad, respectively. The series covered a tilt range from −70° to +74° and using a tilt increment of 2° (Fischione model 2020 single tilt tomography holder). After the first series, which from now on for the sake of simplicity we will refer to as series A, the grid was flipped over 180°, and a second tilt series was acquired (series B) within a tilt range from −74° to +72° and a tilt increment of 2°. In both cases, the beam current was set to 70 pA. A schematic representation of the procedure is shown in Figure 1. Images were aligned with each other by using a phase correlation implemented in Matlab.[23] The aligned series were reconstructed using the simultaneous iterative reconstruction technique (SIRT) implemented in the ASTRA toolbox and the sparse sphere reconstruction (SSR) algorithm.[12,24,25]

*Fusion of Two Image Volumes.* Once the two reconstructions are obtained, they need to be combined into 1 data set. Image volume fusion is a process that aims to combine 3D image volumes so that all the salient information is put together into a single 3D volume suitable for human perception or further processing. Since our objective is to merge two 3D images of the assembly of NPs, each reconstructed from a different tilt-series, image volume fusion is necessary to combine these two reconstructions into a single 3D image volume. In principle, we want to apply *monomodal* image fusion, where the goal is to fuse multiple images with different blurred regions into an image with minimized blurring artifacts.[26] To achieve this objective, we extend the Wavelet-based image fusion,[27,28] commonly used for fusing 2D images, to 3D image volume fusion.[29] Figure 2 demonstrates this image fusion process. The approach aims to take advantage of multiresolution image decomposition schemes and combine their decomposition to obtain the fused images. Multiresolution image decomposition schemes, such as wavelet transform, allow the fused image to retain all the salient features of both images.

We briefly describe the wavelet-based image fusion process here. A 3D wavelet transform decomposes the image $I$ into various bands, i.e., $\mathcal{W}(I) = \{X^{1,1}, ..., X^{p,q}, ..., X^{N,8}\}$, with each $Y^{p,q}$ consisting of wavelet coefficients corresponding to the image at a specific scale and orientation. Once we decompose the images $I$ and $J$, we merge these coefficients using a simple rule to generate the wavelet decomposition of fused volume:

$$Z^{p,q} = \max(X^{p,q}, Y^{p,q}), \text{ for } p = 1, ..., N, q = 1, ..., 8$$

where $\mathcal{W}(I) = \{X^{1,1}, ..., X^{p,q}, ..., X^{N,8}\}$, and $\mathcal{W}(J) = \{Y^{1,1}, ..., Y^{p,q}, ..., Y^{N,8}\}$. Although we show a simple


https://doi.org/10.1021/acs.jpcc.1c08478
J. Phys. Chem. C 2021, 125, 26240−26246

rule to merge these coefficients, a more sophisticated masking-based rule is used in practice to obtain stable coefficients.[27] Finally, these resulting wavelet coefficients can be inverted to obtain the final fused volume $K$ as follows:

$$\mathcal{W}^{-1}(\{Z^{1,1}, ..., Z^{p,q}, ..., Z^{N,8}\}) = K$$

## RESULTS

To demonstrate our approach, a close-packed assembly of spherical Au NPs with a total diameter of 165 nm was used. An HAADF-STEM image of the assembly is provided in Figure 3.

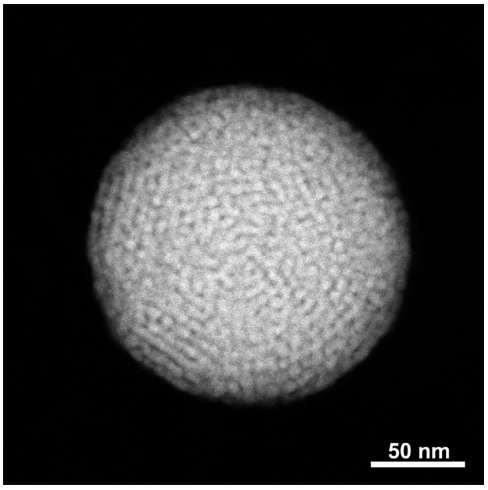


**Figure 3.** HAADF-STEM image of an assembly of spherical Au NPs used for the acquisition of electron tomography series.

For this sample, a HAADF-STEM tilt series was acquired and reconstructed using the SIRT algorithm (see Materials and Methods for more details). A 3D visualization of the SIRT reconstruction and slices through the reconstructed volume are presented in part a of Figure 4a and parts b–d of Figure 4. Figure 4b shows an *XY* orthoslice through the middle of the reconstructed volume, and a strong blurring at the upper half part of the volume can be observed (indicated by a white arrow). This artifact is caused by multiple scattering of the electrons inside the specimen due to the high atomic number of the individual Au NPs and the very compact structure of the assembly. This results in the broadening of the electron beam with increasing penetration depth.

After acquiring the first series (series A), the TEM grid was flipped over 180°, and a second tilt series was acquired (series B; see Figure 1). A 3D visualization of the SIRT reconstruction of series B together with slices through the reconstructed volume is presented in Figure 4e and Figure 4f–h. By comparing the orthoslices in Figure 4, parts b and f, it is evident that the artifact is present at the opposite side of the reconstructed volume. This is also clearly appreciated from a comparison between orthoslices acquired from the upper and lower parts of the two reconstructed volumes along the ZY plane, presented in parts c and d of Figure 4 and parts g and h of Figure 4, respectively.

After aligning both reconstructions from series A and B to each other, we merged them through the image volume fusion process described earlier. For our numerical experiments, we use the Haar wavelet for image decomposition.[30] This wavelet family provides one of the sparsest coefficients for electron tomography images.[31] A 3D visualization of the merged SIRT reconstruction together with orthoslices through the recon-

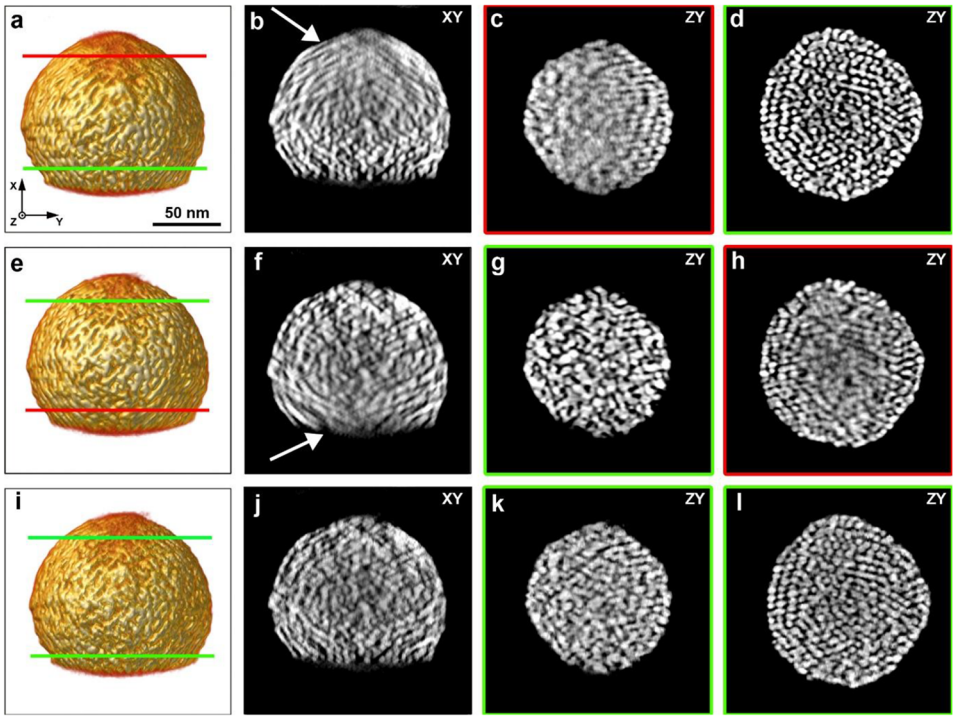


**Figure 4.** 3D visualizations of the SIRT reconstructions (a) series A, (e) series B, and (i) the combined tilt series. The electron beam exit surface is on the top at part a and at the bottom at part e, denoted by the solid red lines. Beam broadening strongly affects these regions, and sample features are poorly resolved at the reconstructed volumes. (b, f, j) Orthoslices along the *XY* plane from the middle part of the reconstructed volumes shown in parts a, e, and i. Orthoslices from the top (c, g, k) and bottom (d, h, l) parts of the reconstructed volumes are shown in parts a, e, and i.



https://doi.org/10.1021/acs.jpcc.1c08478
J. Phys. Chem. C 2021, 125, 26240–26246

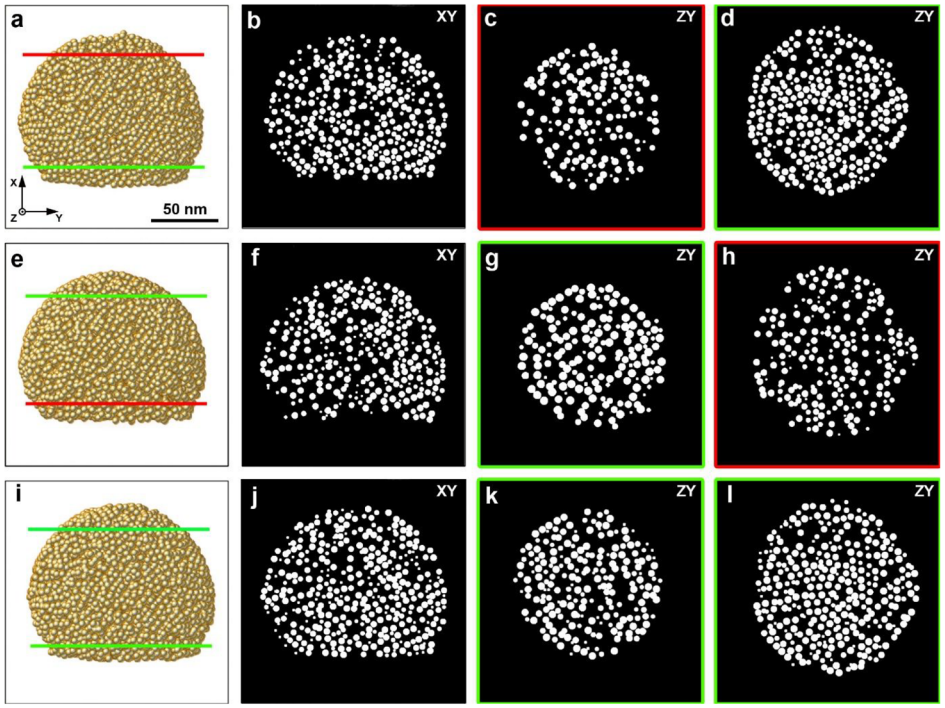


**Figure 5.** 3D visualizations of the SSR reconstructed volumes of (a) series A, (e) series B, and (i) the combined tilt series. The electron beam exit surface is on the top at part a and at the bottom at part e, denoted by the solid red lines. Orthoslices from the upper (c, g, k) and lower (d, h, l) parts of the reconstructed volumes are shown in parts a, e, and i. When comparing part c with part g and part d with part h, noticeable discrepancies in the number and position of detected NPs can be observed.

structed volume are shown in part i and parts j–l of Figure 4, respectively.

Typically, after a 3D reconstruction, a segmentation step is required to quantify the results. Hereby, one tries to find a correspondence between the different intensities in the projection images and the different gray values in the reconstruction. The procedure can be done either manually or in an automatic fashion using a threshold. However, if the number of particles in the assembly increases and the interparticle distance is close to or less than the 3D resolution of the tomography experiment, segmentation, even manually, becomes subjective and quantification unreliable.[32]

To overcome this problem, we recently developed a novel approach for the quantitative 3D characterization of assemblies of spherical NPs, combining the 3D reconstruction and segmentation in a single step.[12] This approach is based on the assumption that all NPs in the assembly have the same (spherical) shape. We therefore refer to this approach as the sparse sphere reconstruction (SSR). By exploiting the assumption of spherical shape, the reconstruction, which is an ill-posed inverse problem, becomes easier to solve and in addition, there is no need to perform a segmentation after the reconstruction. Indeed, the main advantage of the SSR approach in this study is that the coordinates of each NP in a given assembly are extracted automatically during the reconstruction. As a consequence, no manual segmentation of the 3D reconstructed data set is required. We have shown the robustness and reliability of the SSR method both in a qualitative and a quantitative manner in different study cases.[13,14,33] In order to quantitatively evaluate the results of the reconstruction based on a single tilt series and the reconstruction obtained by combining two series, we compared the number of Au NPs in each reconstruction.

The SSR algorithm was initially applied to series A and B separately, and the result is presented in Figure 5. Although it visually appears that the NPs are reliably detected, in practice, the result is strongly affected by the blurring artifacts described above. This can be confirmed by a noticeable difference in the number of detected particles from the reconstructions of series A and B, which was 6988 and 6092, respectively. This difference is mainly related to the nonuniform shape of the assembly, induced by the expected slight flattening of the volume during the drying process after deposition on the TEM grid. This flattened part of the volume (indicated by a white arrow in Figure 4f) contains more particles compared to the round top part. In series B, where the flattened part is affected by blurring, an underestimation of the detected number of particles is expected after quantification. Furthermore, when comparing orthoslices (Figure 5, part c with part g, and Figure 5, part d with part h, respectively) from the same parts of the volumes obtained from series A and B, large discrepancies can be observed. For example, in Figure 5h, where an orthoslice from the bottom part of the reconstructed volume of series B is presented, many particles are not detected, leaving voids in the orthoslice.

The SSR technique was applied to the merged volume (A + B) as well, and the result is presented in Figure 5j, where an orthoslice through the SSR reconstructed volume is shown. In this case, due to the pronounced reduction of the beam broadening induced reconstruction artifacts, a higher quality reconstruction could be obtained, allowing us to detect the highest amount of particles, 7116 in total.

## DISCUSSION

Blurring in the reconstructed volume of thick specimens might be due to the depth of field, in case it is smaller than the size of



https://doi.org/10.1021/acs.jpcc.1c08478
J. Phys. Chem. C 2021, 125, 26240−26246

the sample.[34] One possibility to overcome this effect is to decrease the convergence angle of the incident electron beam in STEM. In order to test the effect of beam convergence on the artifact observed in parts b and f of Figures 4, we acquired a tomography tilt series from another similar assembly of NPs, using 8 mrad, the semiconvergence angle used for the acquisition of the tilt series in the current study, and 1.5 mrad. The outcome of the experiments is presented in Figure 6. Although a convergence angle of 1.5 mrad corresponds to a

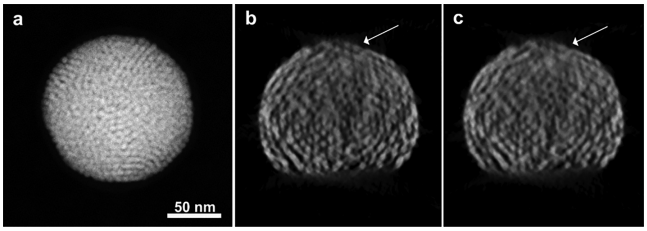


**Figure 6.** (a) HAADF-STEM image of an assembly of spherical Au NPs used for the acquisition of electron tomography series. The orthoslices from the reconstructed volumes of the series using a semiconvergence angle of (b) 8 mrad and (c) 1.5 mrad. The exit surface of the electron beam is at the top of the orthoslices denoted by the white arrows.

sufficiently large depth of field (530 nm)[34] in comparison to the size of the investigated assembly (140 nm), we observe that blurring is still present at the exit surface of the electron beam (white arrows in Figures 6, parts b and c). Furthermore, the 3D spatial resolution was found to be worse in comparison to that using 8 mrad. This is not surprising when using an almost parallel beam in STEM. This experiment demonstrates that the blurring we observed in all reconstructions in our work are related to beam broadening due to the thickness of the structure and high Z number of the individual NPs.

In a different study by Hovden et al., the acquisition of through−focal series of 26 images at every tilt angle was proposed. This approach was successful in overcoming blurring in the reconstructions of thick specimens, caused by a limited depth of field in aberration-corrected STEM.[35] However, through-focal tomography increases the exposure of the sample to the electron beam, which may lead to damage of the sample under investigation. In contrast, our methodology only requires one image at a given tilt angle and can be combined with a fast acquisition scheme where a tilt series is acquired in less than 6 min during continuous or incremental tilting of the TEM holder.[36] We therefore believe that the approach we proposed here can be a useful method to investigate the 3D structure of large assemblies as well as compact assemblies consisting of elements with a high atomic number *Z*.

## CONCLUSIONS

In this work, we proposed a general approach to minimize beam broadening related artifacts present in the 3D reconstruction of thick crystalline samples. We showed an improved acquisition method by obtaining a second tilt series after flipping a thick and compact assembly of spherical Au NPs over 180° around the axis perpendicular to the axis of the holder. By merging the two reconstructions, we overcome blurring artifacts in the reconstructed volume. The coordinates of the Au NPs in the assembly were extracted using the SSR algorithm. We believe that the advantages of our approach will be of great benefit not only for the quantitative 3D investigation of assemblies of spherical NPs and/or assemblies with high atomic number *Z*, but also of assemblies of anisotropic NPs. In this manner, the position and orientation of the building blocks can be determined in a reliable manner. Furthermore, when combined with a fast tilt series acquisition scheme, it may be used for the investigation of beam sensitive materials, such as for example metallic NPs-loaded porous structures used in catalysis.[37]

## AUTHOR INFORMATION

### Corresponding Author

**Sara Bals** − *EMAT, University of Antwerp, 2020 Antwerp, Belgium;* orcid.org/0000-0002-4249-8017; Email: sara.bals@uantwerpen.be

### Authors

**Thomas Altantzis** − *EMAT, University of Antwerp, 2020 Antwerp, Belgium; ELCAT, University of Antwerp, 2610 Wilrijk, Belgium;* orcid.org/0000-0002-4940-7931

**Da Wang** − *EMAT, University of Antwerp, 2020 Antwerp, Belgium; Soft Condensed Matter, Debye Institute for Nanomaterials Science, Utrecht University, 3584 CC Utrecht, The Netherlands*

**Ajinkya Kadu** − *EMAT, University of Antwerp, 2020 Antwerp, Belgium; Computational Imaging, Centrum Wiskunde & Informatica, 1098 XG Amsterdam, The Netherlands*

**Alfons van Blaaderen** − *Soft Condensed Matter, Debye Institute for Nanomaterials Science, Utrecht University, 3584 CC Utrecht, The Netherlands*

Complete contact information is available at: https://pubs.acs.org/10.1021/acs.jpcc.1c08478

### Author Contributions

⊥T.A., D.W., and A.K. contributed equally. T.A. and S.B. initiated the experimental part of the project. T.A. performed all the TEM experiments. D.W. synthesized the samples under the supervision of A.v.B and performed SIRT reconstructions under the supervision of S.B. A.K. merged the two volumes using the wavelet-based image fusion process and performed the SSR tomographic reconstructions under the supervision of S.B. The manuscript was written through contributions of all authors. All authors have given approval to the final version of the manuscript.

### Notes

The authors declare no competing financial interest.

## ACKNOWLEDGMENTS

This work was supported by the European Research Council (Grant No. 815128-REALNANO to S.B.). T.A. acknowledges the University of Antwerp Research fund (BOF). D.W. and A.v.B. acknowledge partial financial support from the European Research Council under the European Union's Seventh Framework Program (FP-2007-2013)/ERC Advanced Grant Agreement 291667 HierarSACol. D.W. acknowledges an Individual Fellowship funded by the Marie Sklodowska-Curie Actions (MSCA) in Horizon 2020 program (Grant 894254 SuprAtom).

## REFERENCES

(1) Hamon, C.; Novikov, S. M.; Scarabelli, L.; Solis, D. M.; Altantzis, T.; Bals, S.; Taboada, J. M.; Obelleiro, F.; Liz-Marzan, L. M.

Collective Plasmonic Properties in Few-Layer Gold Nanorod Supercrystals. *ACS Photonics* **2015**, *2* (10), 1482−1488.
(2) Guo, S.; Dong, S. Metal Nanomaterial-Based Self-Assembly: Development, Electrochemical Sensing and SERS Applications. *J. Mater. Chem.* **2011**, *21* (42), 16704.
(3) Kim, K.; Shin, D.; Kim, K. L.; Shin, K. S. Electromagnetic Field Enhancement in the Gap between Two Au Nanoparticles: The Size of Hot Site Probed by Surface-Enhanced Raman Scattering. *Phys. Chem. Chem. Phys.* **2010**, *12* (15), 3747−3752.
(4) Guo, S.; Sun, S. FePt Nanoparticles Assembled on Graphene as Enhanced Catalyst for Oxygen Reduction Reaction. *J. Am. Chem. Soc.* **2012**, *134* (5), 2492−2495.
(5) Xu, Y.; Hou, S.; Liu, Y.; Zhang, Y.; Wang, H.; Zhang, B. Facile One-Step Room-Temperature Synthesis of Pt3Ni Nanoparticle Networks with Improved Electro-Catalytic Properties. *Chem. Commun.* **2012**, *48* (21), 2665.
(6) Pileni, M. P. 2D Superlattices and 3D Supracrystals of Metal Nanocrystals: A New Scientific Adventure. *J. Mater. Chem.* **2011**, *21* (42), 16748.
(7) Pileni, M.-P. The Role of Soft Colloidal Templates in Controlling the Size and Shape of Inorganic Nanocrystals. *Nat. Mater.* **2003**, *2* (3), 145−150.
(8) Sánchez-Iglesias, A.; Grzelczak, M.; Altantzis, T.; Goris, B.; Pérez-Juste, J.; Bals, S.; Van Tendeloo, G.; Donaldson, S. H.; Chmelka, B. F.; Israelachvili, J. N.; et al. Hydrophobic Interactions Modulate Self-Assembly of Nanoparticles. *ACS Nano* **2012**, *6*, 11059−11065.
(9) Yang, Y.; et al. Scalable Assembly of Crystalline Binary Nanocrystal Superparticles and Their Enhanced Magnetic and Electrochemical Properties. *J. Am. Chem. Soc.* **2018**, *140*, 15038−15047.
(10) Galván-Moya, J. E.; Altantzis, T.; Nelissen, K.; Peeters, F. M.; Grzelczak, M.; Liz-Marzán, L. M.; Bals, S.; Van Tendeloo, G. Self-Organization of Highly Symmetric Nanoassemblies: A Matter of Competition. *ACS Nano* **2014**, *8*, 3869−3875.
(11) Altantzis, T.; Goris, B.; Sánchez-Iglesias, A.; Grzelczak, M.; Liz-Marzán, L. M.; Bals, S. Quantitative Structure Determination of Large Three-Dimensional Nanoparticle Assemblies. *Part. Part. Syst. Charact.* **2013**, *30* (1), 84−88.
(12) Zanaga, D.; Bleichrodt, F.; Altantzis, T.; Winckelmans, N.; Palenstijn, W. J.; Sijbers, J.; de Nijs, B.; van Huis, M. A.; Sánchez-Iglesias, A.; Liz-Marzán, L. M.; et al. Quantitative 3D Analysis of Huge Nanoparticle Assemblies. *Nanoscale* **2016**, *8* (1), 292−299.
(13) Wang, D.; Dasgupta, T.; van der Wee, E. B.; Zanaga, D.; Altantzis, T.; Wu, Y.; Coli, G. M.; Murray, C. B.; Bals, S.; Dijkstra, M.; et al. Binary Icosahedral Clusters of Hard Spheres in Spherical Confinement. *Nat. Phys.* **2021**, *17* (1), 128−134.
(14) Wang, D.; van der Wee, E. B.; Zanaga, D.; Altantzis, T.; Wu, Y.; Dasgupta, T.; Dijkstra, M.; Murray, C. B.; Bals, S.; van Blaaderen, A. Quantitative 3D Real-Space Analysis of Laves Phase Supraparticles. *Nat. Commun.* **2021**, *12* (1), 3980.
(15) Wang, D.; Hermes, M.; Kotni, R.; Wu, Y.; Tasios, N.; Liu, Y.; De Nijs, B.; Van Der Wee, E. B.; Murray, C. B.; Dijkstra, M.; et al. Interplay between Spherical Confinement and Particle Shape on the Self-Assembly of Rounded Cubes. *Nat. Commun.* **2018**, *9* (1), 2228.
(16) Midgley, P. A.; Weyland, M. 3D Electron Microscopy in the Physical Sciences: The Development of Z-Contrast and EFTEM Tomography. *Ultramicroscopy* **2003**, *96* (3−4), 413−431.
(17) Boneschanscher, M. P.; Evers, W. H.; Geuchies, J. J.; Altantzis, T.; Goris, B.; Rabouw, F. T.; van Rossum, S.a P.; van der Zant, H. S. J.; Siebbeles, L. D. A; Van Tendeloo, G.; et al. Long-Range Orientation and Atomic Attachment of Nanocrystals in 2D Honeycomb Superlattices. *Science* **2014**, *344*, 1377−1380.
(18) Udayabhaskararao, T.; Altantzis, T.; Houben, L.; Coronado-Puchau, M.; Langer, J.; Popovitz-Biro, R.; Liz-Marzán, L. M.; Vukovic, L.; Král, P.; Bals, S.; et al. Tunable Porous Nanoallotropes Prepared by Post-Assembly Etching of Binary Nanoparticle Superlattices. *Science* **2017**, *358* (6362), 514−518.
(19) Gentsch, P.; Gilde, H.; Reimer, L. Measurement of the Top Bottom Effect in Scanning Transmission Electron Microscopy of Thick Amorphous Specimens. *J. Microsc.* **1974**, *100* (1), 81−92.
(20) Hohmann-Marriott, M. F.; Sousa, A. A.; Azari, A. A.; Glushakova, S.; Zhang, G.; Zimmerberg, J.; Leapman, R. D. Nanoscale 3D Cellular Imaging by Axial Scanning Transmission Electron Tomography. *Nat. Methods* **2009**, *6* (10), 729−731.
(21) Zheng, N.; Fan, J.; Stucky, G. D. One-Step One-Phase Synthesis of Monodisperse Noble-Metallic Nanoparticles and Their Colloidal Crystals. *J. Am. Chem. Soc.* **2006**, *128* (20), 6550−6551.
(22) Mason, T. G.; Bibette, J. Shear Rupturing of Droplets in Complex Fluids. *Langmuir* **1997**, *13* (17), 4600−4613.
(23) Altantzis, T.; Lobato, I.; De Backer, A.; Béché, A.; Zhang, Y.; Basak, S.; Porcu, M.; Xu, Q.; Sánchez-Iglesias, A.; Liz-Marzán, L. M.; et al. Three-Dimensional Quantification of the Facet Evolution of Pt Nanoparticles in a Variable Gaseous Environment. *Nano Lett.* **2019**, *19* (1), 477−481.
(24) Palenstijn, W. J.; Batenburg, K. J.; Sijbers, J. Performance Improvements for Iterative Electron Tomography Reconstruction Using Graphics Processing Units (GPUs). *J. Struct. Biol.* **2011**, *176* (2), 250−253.
(25) van Aarle, W.; Palenstijn, W. J.; De Beenhouwer, J.; Altantzis, T.; Bals, S.; Batenburg, K. J.; Sijbers, J. The ASTRA Toolbox: A Platform for Advanced Algorithm Development in Electron Tomography. *Ultramicroscopy* **2015**, *157*, 35−47.
(26) Stathaki, T. *Image Fusion: Algorithms and Applications*; Elsevier: 2011.
(27) Li, H.; Manjunath, B. S.; Mitra, S. K. Multisensor Image Fusion Using the Wavelet Transform. *Graph. Model. Image Process.* **1995**, *57* (3), 235−245.
(28) Pajares, G.; Manuel de la Cruz, J. A Wavelet-Based Image Fusion Tutorial. *Pattern Recognit.* **2004**, *37* (9), 1855−1872.
(29) Nikolov, S. G.; Bull, D. R.; Canagarajah, C. N.; Halliwell, M.; Wells, P. N. T. Image Fusion Using a 3-D Wavelet Transform*7th International Conference on Image Processing and its Applications*; IEE: 1999; pp 235−239.
(30) Nikolov, S. Wavelets for Image Fusion. In *Wavelets in Signal and Image Analysis*; Springer: 2001; Vol. *19*, pp 213−241.
(31) Donati, L.; Nilchian, M.; Trépout, S.; Messaoudi, C.; Marco, S.; Unser, M. Compressed Sensing for STEM Tomography. *Ultramicroscopy* **2017**, *179*, 47−56.
(32) Heidari, H.; Van den Broek, W.; Bals, S. Quantitative Electron Tomography: The Effect of the Three-Dimensional Point Spread Function. *Ultramicroscopy* **2013**, *135*, 1−5.
(33) Yang, Z.; Altantzis, T.; Zanaga, D.; Bals, S.; Tendeloo, G.; Pileni, M.-P. Supracrystalline Colloidal Eggs: Epitaxial Growth and Freestanding Three-Dimensional Supracrystals in Nanoscaled Colloidosomes. *J. Am. Chem. Soc.* **2016**, *138* (10), 3493−3500.
(34) Hyun, J. K.; Ercius, P.; Muller, D. A. Beam Spreading and Spatial Resolution in Thick Organic Specimens. *Ultramicroscopy* **2008**, *109* (1), 1−7.
(35) Hovden, R.; Ercius, P.; Jiang, Y.; Wang, D.; Yu, Y.; Abruña, H. D.; Elser, V.; Muller, D. A. Breaking the Crowther Limit: Combining Depth-Sectioning and Tilt Tomography for High-Resolution, Wide-Field 3D Reconstructions. *Ultramicroscopy* **2014**, *140*, 26−31.
(36) Albrecht, W.; Bals, S. Fast Electron Tomography for Nanomaterials. *J. Phys. Chem. C* **2020**, *124* (50), 27276−27286.
(37) Arenas-Vivo, A.; Rojas, S.; Ocaña, I.; Torres, A.; Liras, M.; Salles, F.; Arenas-Esteban, D.; Bals, S.; Ávila, D.; Horcajada, P. Ultrafast Reproducible Synthesis of a Ag-nanocluster@MOF Composite and Its Superior Visible-Photocatalytic Activity in Batch and in Continuous Flow. *J. Mater. Chem. A* **2021**, *9* (28), 15704−15713.


https://doi.org/10.1021/acs.jpcc.1c08478
J. Phys. Chem. C 2021, 125, 26240−26246